Intermetallics 156 (2023) 107853

Contents lists available at ScienceDirect

Intermetallics

journal homepage: www.elsevier.com/locate/intermet

Primary and secondary phase separation in Cu–Zr–Al bulk metallic glass by control of quenching conditions

Y. Zhang, S. Ren, S. Sohrabi **, J. Ma *

Shenzhen Key Laboratory of High Performance Nontraditional Manufacturing, College of Mechatronics and Control Engineering, Shenzhen University, Shenzhen, 518060, China

ARTICLE INFO

Keywords:
Bulk metallic glass
Phase separation
Structural relaxation
Electron microscopy
Chemical heterogeneities

ABSTRACT

Here, we report primary and secondary nanoscale phase separation in $Cu_{46}Zr_{46}Al_8$ (at.%) bulk metallic glass (BMG) achieved by altering the casting temperature. The BMG rods were cast by using the melting currents of 160 A and 220 A which provide, respectively, higher and lower cooling rates. The transmission electron microscopy and energy-dispersive X-ray analysis revealed that the higher cooling rate conditions brings a primary phase separation of nanoscale Cu-rich amorphous regions which are evenly dispersed in the Cu-depleted amorphous matrix phase. However, lower cooling rates results in a bimodal microstructure comprising coarsened primary-separated nanograins and very fine secondary-separated nanograins throughout the amorphous matrix containing nanocrystals of smaller than 5 nm in size. This unique microstructure developed under lower cooling rates gives lower relaxation enthalpy, higher short-range ordering, and enhanced strain-hardening. Our study emphasizes the significant role of casting temperature on controlling the morphology of nanoscale phase separation in BMGs.

1. Introduction

Bulk metallic glasses (BMGs) have high strength, high elastic limit, and excellent corrosion resistance due to their amorphous structure, making them a potential candidate to serve as structural materials. The common drawback in the mechanical performance of monolithic BMGs is poor plasticity due to strain softening and the localization of deformation in shear bands. To address this, introducing micro/nano-scale heterogeneities to the microstructure of BMGs has been developed as an effective approach to nucleate multiple shear bands and impede their propagation [1–5]. The heterogeneities can be structural, such as micrometer-sized crystalline reinforcements [4,6,7] and nanoscale crystals embedded in the amorphous matrix [8,9], or they can have a compositional (chemical) origin [2,10–12]. A pronounced form of chemical heterogeneity is liquid phase separation [13] in which the liquid decomposes into two liquid structures during cooling because the chemical composition is in the range of a miscibility gap and consequently, the two amorphous phases are formed [14]. Phase separation can significantly enhance the glass-forming ability (GFA) and alter the crystallization pathways in BMGs [15]. The nano-scale phase separation in BMGs enjoys great advantages in terms of enhanced plasticity and improved work-hardening compared to monolithic BMGs [2,16,17].

Since the discovery of BMGs in 1990s, a large variety of BMG alloy systems have been developed, including Zr- [18], Pd- [19], Cu- [20], La- [21], and CuZr-based [17] BMGs [22]. The ternary Cu–Zr–Al BMGs based on $Cu_{50}Zr_{50}$ binary system are of particular interest due to their simplicity and nontoxicity, good mechanical properties, high GFA, and high thermal stability against crystallization [12,23,24]. Phase separation in Cu–Zr–Al alloy system is theoretically unexpected as the atomic pairs all have negative mixing enthalpies and phase separation in this alloy system is mainly achieved by minor addition of elements having relatively large positive mixing enthalpies (such as Fe [25] and Gd [26]). However, there are few reports confirming the occurrence of phase separation in the as-cast Cu–Zr–Al BMGs [16,27], which is thermodynamically attributed to local narrow miscibility gap appeared during rapid cooling of the melt [13].

While quenching condition is one of the main factors influencing the microstructural evolution during phase separation of BMGs [13], the cooling rate effects on the morphology of phase separated regions in Cu–Zr–Al BMGs are not well explored. In a recent report, it was shown

* Corresponding author.
** Corresponding author.
E-mail addresses: ssohrabi@szu.edu.cn (S. Sohrabi), majiang@szu.edu.cn (J. Ma).

https://doi.org/10.1016/j.intermet.2023.107853
Received 26 December 2022; Received in revised form 28 January 2023; Accepted 11 February 2023
Available online 15 February 2023

that when the mold temperature decreases from 298 K to 193 K during copper-mold suction casting of BMG, the compositional contrast between Cu-rich and Zr-rich phase separated regions becomes more pronounced as a consequence of higher cooling rates achieved. In the present study, we show that the quenching conditions could even have a more noticeable effect on the phase separation in the as-cast $Cu_{46}Zr_{46}Al_8$ BMG, yielding a clear transition from primary to secondary phase separation when the melt temperature is increased.

2. Materials and methods

The nominal composition of the alloy system used in this study was $Cu_{46}Zr_{46}Al_8$ (at.%). The starting high-purity (>99.5%) elements were melted in a vacuum arc melting furnace under the protection of Ar and the ingot was remelted for 4 times to ensure the homogeneity. The BMG rods of Ø3 × 70 mm were prepared by suction casting into a water-cooled copper mold. Two different cooling rates (CRs) were used during suction casting by adjusting the melting current to the values of 160 A and 220 A. As all other casting parameters were kept unchanged, including the ingot weight, melting duration, and the mold temperature, a higher melting current is expected to result in higher melt temperatures (superheats) and consequently lower CRs [27,28].

The amorphicity of as-cast samples were analyzed by the X-ray diffraction (XRD, BrukerD8 instrument with Cu-K_α radiation) analysis. The differential scanning calorimetry (DSC, Perkin-Elmer DSC 8000 instrument) under Ar atmosphere was used to investigate thermal properties in the cast samples. A heating rate of 0.33 K $s^{-1}$and a cooling rate of 0.83K s^{-1} were used. The microstructure of cast samples was characterized by the transmission electron microscopy (TEM, Fei Tian Themis operating at 200 kV) equipped with energy-dispersive X-ray spectroscopy (EDS). The TEM samples were prepared by focused ion beam (FIB) on FEI Scios SEM/FIB dual beam system. A protective Pt layer was deposited on the samples during the FIB sample preparation. The EDS analysis were performed in scanning mode (STEM) using a high-angle annular dark-field (HAADF) detector. The mechanical properties in the cast samples were investigated by Vickers microhardness (MH-5L, Everone) and instrumented nanoindentation (Bruker TI 980). The Vickers microhardness was carried out by applying a static load of 300 g and applying a dwell time of 5 s, and making a minimum of 15 measurements for each sample. The nanoindentation experiments were conducted by using a Berkovich triangular pyramid indenter with a tip radius of 20 nm and applying a maximum loading of 10 mN with a loading rate of 0.5 mN s^{-1}. At least 10 indentations were performed for each sample.

3. Results and discussion

Fig. 1 shows the XRD patterns of the as-cast rods prepared at different melting currents of 220 A (low CR) and 160 A (high CR). We should here note that the CRs achieved by altering the casting temperature may have the same order of magnitude [29] and the terms *low* and *high* CRs denote the comparative aspects of our study. As can be seen, the diffractions pattens in both samples are broad peaks which is characteristic of an amorphous structure. The lack of sharp crystalline peaks in the XRD patterns implies a fully amorphous structure within the detection limits of the XRD technique. The peak position ($2\theta_p$) and the full-width at half maximum (FWHM) of amorphous peaks can be analyzed by fitting a Gaussian function to the XRD patterns in Fig. 1. While the values of $2\theta_p$ for both samples are identical ($2\theta_p = 38.73° \pm 0.014°$), the calculated values of FWHM for the samples cast at the currents of 220 A and 160 A are, respectively, $6.12° \pm 0.050°$ and $6.41° \pm 0.045°$. The smaller FWHM suggests achieving higher degree of structural ordering in the sample cast by lower CRs (220 A) [30].

The DSC traces of the as-cast rods during continuous heating at the heating rate of 0.33 K s^{-1} are shown in Fig. 2(a). The distinct glass transition signals in both samples followed by the sharp crystallization

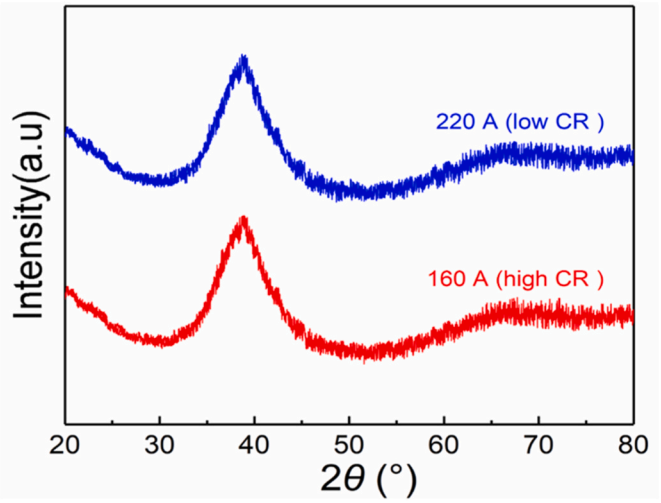

Fig. 1. The XRD patterns of 220 A (low CR) and 160 A (high CR) samples.

peaks confirm the amorphous nature of the as-cast rods. The values of the onset temperature of glass transition (T_g), the onset temperature crystallization (T_x), the width of supercooled liquid region ($\Delta T_x = T_x - T_g$), and the crystallization enthalpy ($\Delta H_{cryst.}$) are extracted from the DSC signals in Fig. 2(a) and summarized in Table 1. It can be seen the values of T_g, T_x, and ΔT_x are almost similar for the both alloys, suggesting that cooling rate does not significantly affect thermal stability of the as-cast BMG rods, as reported before [27]. However, the values of $\Delta H_{cryst.}$ in the sample cast under 160 A (high CR) is 57 J g^{-1}, which is ~20% higher than that in the 220 A (low CR) sample. The smaller $\Delta H_{cryst.}$ suggests that casting of the BMG rods at lower CRs lowers degree of amorphicity, probably due to increased short-range and medium range ordering [31,32] and partial crystallization [33].

The extent of structural relaxation can be quantitatively determined from the DSC traces. The broad specific heat exotherm preceding glass transition of the as-cast rods (as shown in Fig. 2(b)) is a characteristic of structural relaxation. As can be seen, the 160 A (high CR) sample has a bigger relaxation exotherm and clearly suggests that higher cooling rate used during rapid quenching of the melt increases the internal energy of the glassy alloy to higher energy (rejuvenated) states [34]. The values of relaxation enthalpy (ΔH_{rel}) for the as-cast rods can be measured by integrating the heat exotherm [11,35–37] and given in Table 1. The data shows that as higher CRs are used by using lower melting current (160 A), the value of ΔH_{rel} reaches to 6.5 J g^{-1}, which is ~47% larger than the value in low CR condition (4.4 J g^{-1}). This finding highlights the fact that the sample cast at higher CR, as it was expected [38], has larger free volume content frozen during rapid quenching of the initial melt.

Fig. 3(a) shows the overall view of a representative TEM sample prepared by the FIB technique. The FIB-ed samples have several advantages over the samples prepared by ion-milling and jet electropolishing. First, a large area of the sample with fairly uniform thickness can be used for microstructural characterizations. Further, irradiation-induced crystallization and also possible artificial contrasts which are misconstrued as phase separation in Cu-Zr based BMGs [39,40] are avoided.

The selected area electron diffraction (SAED) patterns of as-cast samples are shown in Fig. 3(b). The SAED patterns of both samples display diffuse halo rings with no spots, which is characteristics of amorphous structure. However, the diffraction ring of the sample cast at the melting current of 220 A (low CR) is sharper than that in the sample cast at the melting current of 160 A (high CR), implying a higher degree of short-range ordering and pointing to the formation of crystals below nanometer levels [16,41]. To further investigate this, we performed high-resolution TEM (HRTEM) analysis on both samples (see Fig. 3 (c) and (d)). It can be observed that both samples show a maze structure

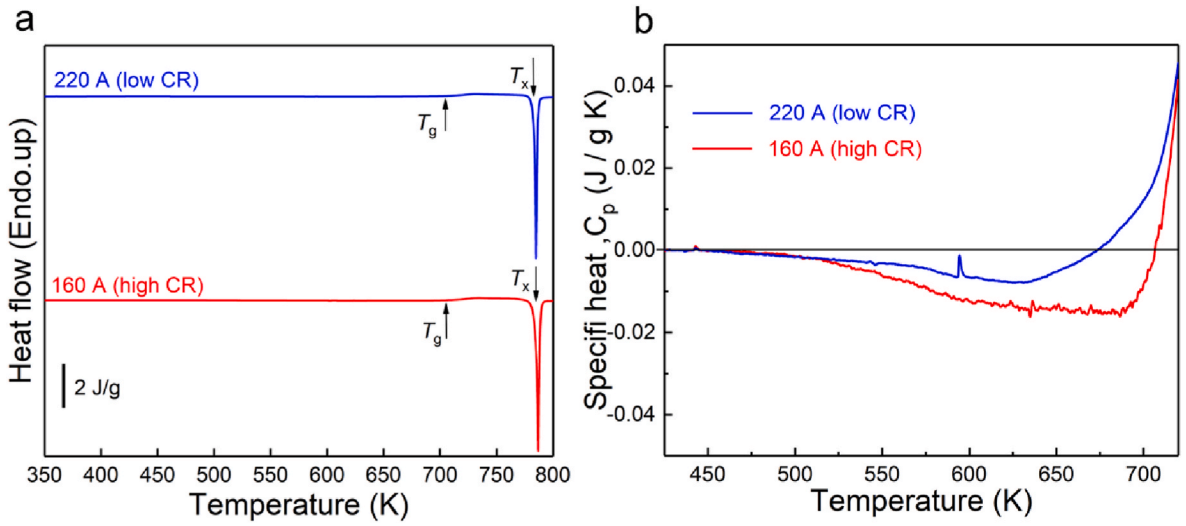

Fig. 2. (a) The DSC traces of as-cast samples. The arrows point to the T_g and T_x. (b) The enlarged view of the exothermic structural relaxation.

Table 1
Thermal properties determined from the DSC measurements. The maximum error for determining T_g and T_x is 2 K.

Sample	T_g (K)	T_x (K)	ΔT_x (K)	$\Delta H_{cryst.}$ (J g^{-1})	ΔH_{rel} (J g^{-1})
220 A (low CR)	704	784	80	47.0	4.4
160A (high CR)	704	785	81	57.0	6.5

with some local regions of uneven contrast, denoting the formation of structural heterogeneities at the atomic length scales. Noticeably, the HRTEM image of the sample prepared at lower CR (Fig. 3 (c)) reveals tiny lattice fringes typical of crystal structure. The size of the precipitated nanocrystals is smaller than 5 nm. However, the HRTEM image of the sample prepared at higher CR (Fig. 3(d)) lacks such lattice fringes. This can also be identified from the Fast Fourier Transformed (FFT) patterns of the HRTEM images (see the insets in Fig. 3 (c) and (d)) where some spots appeared on the main halo in 220 A (low CR) sample, denoting the existence of nanoscale crystals [17]. The diffraction spots in the FFT pattern consist of atomic planes oriented along the [15 6 1] zone axis together with a diffuse halo, denoting the formation of $Cu_{10}Zr_7$ phase belonging to the space group *Cmca* with a tetragonal unit cell of $a = 12.7$ Å and $b = c = 9.4$ Å [42]. As evidenced by lower $\Delta H_{cryst.}$ values in 220 A (low CR) sample, these pre-existing nanocrystals facilitate the crystallization process [33,43].

In order to further evaluate the effects of quenching conditions on the microstructure, the TEM bright-field images of the as-cast samples

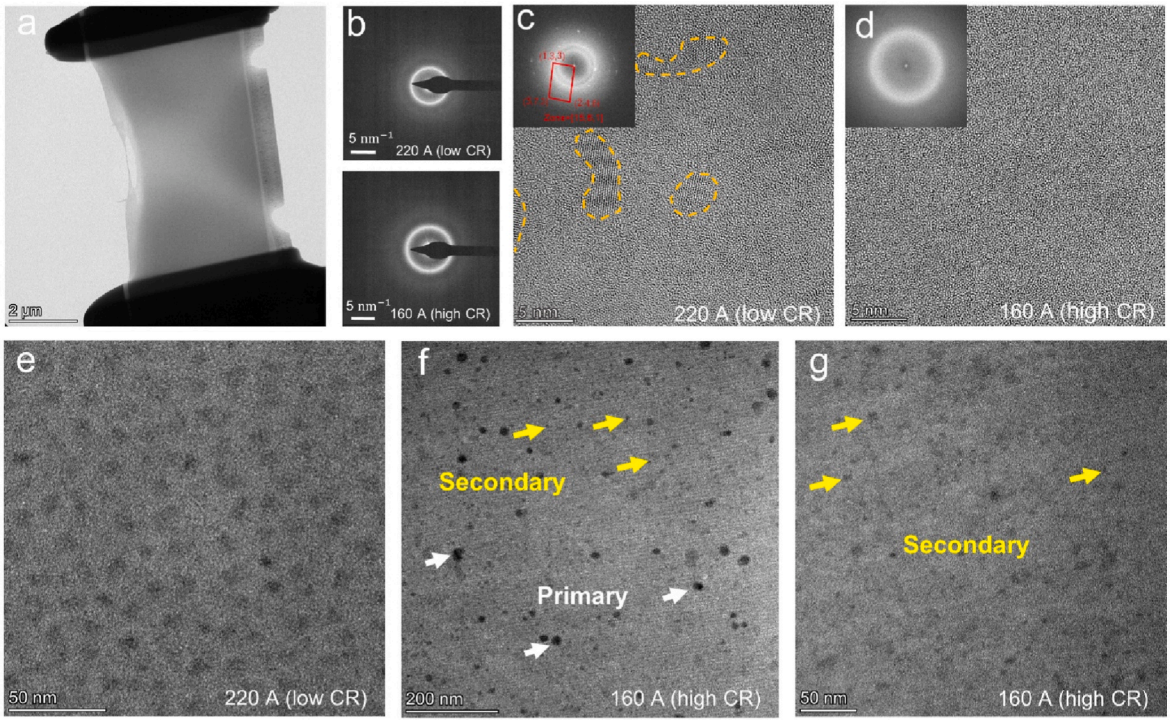

Fig. 3. (a) An overall view of TEM sample prepared by FIB method. (b) The SAED patterns taken from 220 A (low CR) and 160 A (high CR) samples. (c) The HRTEM image of sample cast under the meting current of 220 A (low CR). (d) The HRTEM image of the sample cast by 160 A melting current. (e) TEM bright-field image at lower magnifications for 160 A (high CR) condition. (f–g) TEM bright-field images at lower magnifications for 220 A (low CR) condition.

are shown in Fig. 3(e–g). It can be seen from the TEM image in Fig. 3 (e) that in the case of higher CRs, spherical or droplet-type nanoscale regions of dark contrast are evenly dispersed throughout the amorphous matrix with a bright contrast. Surprisingly, the TEM image in Fig. 3(f) shows that when the glass is quenched at lower CRs (melting current of 220 A), the distribution of the spherical droplets across the amorphous matrix becomes bimodal, comprising larger spheres of darker contrasts with uneven distribution which are noted as primary, and smaller spheres of brighter contrasts with uniform distribution noted as secondary. The small-sized (secondary) spherical contrasts are more easily detectable at higher magnifications, as shown in Fig. 3 (g). The average size of the dark contrast regions is measured from TEM images and are shown in Fig. 4. The primary contrasts in 160 A (high CR) have an average size of ~13 nm, but the brighter contrasts in 220 A (low CR) sample show a bimodal distribution. While the larger sized primary regions have a wide size distribution (average size of ~21 nm), the smaller sized secondary regions have a narrower size distribution with an average size of ~8 nm.

The micro/nano-scale droplet-type morphology is a typical microstructural feature representing phase separation in BMGs [13]. We conducted EDS analysis to ascertain whether the spherical contrasts observed for the cast samples have a chemical origin. The HAADF-STEM images and the corresponding EDS maps of both samples are given in Fig. 5. As can be seen, the brighter contrast regions with higher density in the HAADF images are comparatively rich in Cu, but Zr and Al atoms appear to be distributed homogenously. The chemical compositions of phase separated regions determined from EDS maps are given in Table 2. While the composition of Cu-depleted regions is almost similar in both samples, the chemistry of the primary-separated regions is affected by the melting current. It can be seen that under low CR condition, the primary-separated Cu-rich regions are comparatively richer in Cu and poorer in Zr content. Further, the concentration of Cu atoms in the secondary-separated Cu-rich regions reaches a maximum of 78 at. %, but the Zr content reduces to values as small as 13 at. %. These values are remarkably deviating from the Zr and Cu contents in the nominal composition (46 at. %).

The observation of Cu-rich amorphous regions dispersed throughout the Cu-depleted amorphous matrix provides conclusive evidence that the contrasts observed in the microstructures of cast samples (Fig. 3 (e–g)) are due to phase separation at nanoscale length scales. While primary phase separation was previously reported in in $Cu_{47.5}Zr_{47.5}Al_5$ BMG and more recently, secondary phase separation was discovered in $Cu_{46}Zr_{46}Al_8$ BMG as tangled patterns of compositional modulation with a mixture of length scales, our results highlight the fact that that the secondary phase separation in Cu–Zr–Al alloy system can be manifested as *distinct* nanograins by varying the quenching conditions.

The phase separation in MG systems develops through two typical microstructures: spherical (droplet-type) and interconnected-type morphologies. While the latter is originated from spinodal decomposition, the former is known to be controlled by a nucleation and growth mechanism. Whether which type of these morphologies is developed strongly depends on the chemical composition and quenching conditions [13]. As the morphology of phase separated regions in our study is spherical (droplet-type), it can be immediately realized that the mechanism of the phase separations observed in this study is nucleation and growth.

We here elaborate on the possible mechanism for the formation of primary and secondary phase separation. First, it should be noted that decomposition of constituent elements in Cu–Zr–Al alloy system with large negative mixing enthalpies among all the atomic pairs may originate from falling of the alloy melt into a local metastable miscibility gap during rapid cooling [13,44]. Upon sufficient undercooling and entering the miscibility gap, there would be a thermodynamic driving force for the primary separation of Cu atoms and precipitation of a new amorphous phase dispersed in the amorphous matrix. When the CR is sufficiently high, the temperature at which the phase separation occurs decreases to quite low temperatures corresponding to the terminal compositions of the tie line in the miscibility gap where there is no driving force for further separation. Therefore, primary-separated regions show a homogenous distribution. However, phase separation at lower CR appears to be more complex. One possible explanation is that under low CR conditions, the phase separation starts at higher initial temperatures within the miscibility gap and the small compositional difference at high temperatures may give higher propensity for multi-stage separations at lower temperatures [27]. This scenario is, nonetheless, unlikely in our case of study since this mechanism should bring a complex network of phase separated regions over a wide range of length scales with smaller compositional difference between phase separated regions at lower CRs [27,45]. However, the compositional data (Table 1) clearly showed that lower CR results in larger difference in Cu concentrations between primary Cu-rich regions and Cu-depleted regions.

A more plausible scenario for observation of primary and secondary phase separation is that during casting at lower CRs, the time for the mass transport is significantly available and the atomic diffusion rate is high. Consequently, the diffusion and coalescence of the primary-separated regions coarsen these nanoregions in order to decrease the interfacial energy. The coarsening of primary-separated phase can be also evidenced by comparing the average size of these regions in low CR (~21 nm) and high CR (~13 nm) conditions, as shown in Fig. 4. In addition, the greater compositional difference between primary Cu-rich regions and Cu-depleted matrix observed for the sample cast at higher melt superheat (low CR condition; see Table 1) may be ascribed to the higher degree of melt undercooling [46] and consequently achieving a wider tie line with more distinct terminal compositions in the miscibility gap. On further cooling, the supersaturation of the primary-separated

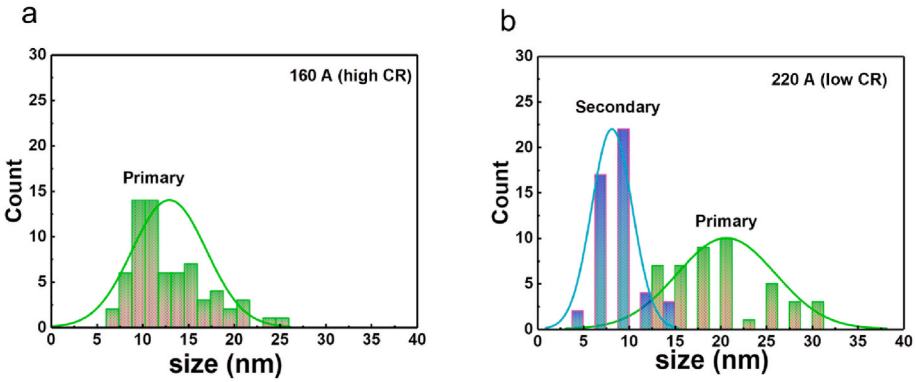

Fig. 4. (a) The size distribution of primary droplet-type contrasts in 160 A (high CR) sample. (b) The size distribution of primary (larger) and secondary (smaller) droplet-type contrasts under 220 A (low CR) conditions.

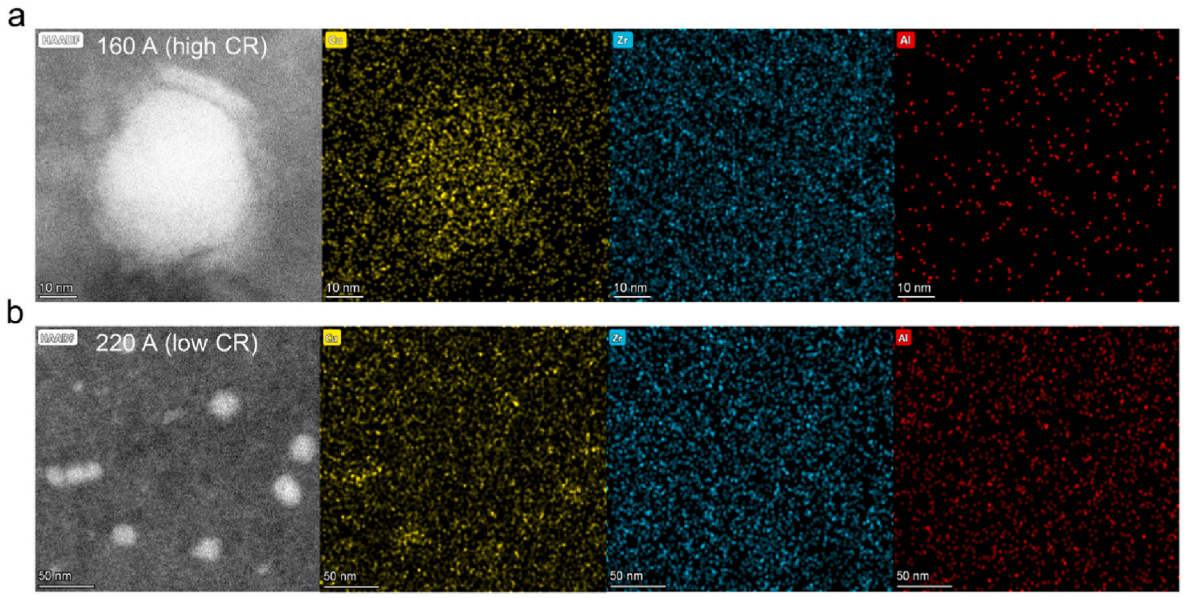

Fig. 5. The HAADF images and EDS mapping of the constituent elements in the STEM mode for (**a**) primary-separated nanoscale regions in the sample cast by the melting current of 160 A (high CR), and (**b**) secondary-separated regions in the sample cast by the melting current of 220 A (low CR).

Table 2
Chemical compositions measured from the EDS maps. The composition of secondary Cu-rich regions corresponds to the small-sized bright contrasts determined from the HAADF image in Fig. 5b. The maximum standard deviation for the determination of composition was ±2 at. %.

Sample	Composition (at. %)		
	Cu-rich (primary)	Cu-rich (secondary)	Cu-depleted
220 A (low CR)	$Cu_{66}Zr_{28}Al_6$	$Cu_{78}Zr_{13}Al_9$	$Cu_{36}Zr_{60}Al_4$
160A (high CR)	$Cu_{57}Zr_{40}Al_3$	n/a	$Cu_{36}Zr_{60}Al_4$

phase and amorphous matrix phase may occur because the atomic diffusion rate at lower temperatures is insufficient to reach equilibrium composition at each temperature, yielding the formation of fine secondary-separated droplets within the melt [13]. Compared to the primary-separated regions, the Cu-rich regions generated during the second separation and the Cu-depleted regions would have much greater compositional difference, as confirmed by with the compositional data in Table 1. This is because the second separation occurs at lower temperatures where the compositions of separated regions are further apart in the miscibility gap.

In order to evaluate the effects of quenching condition and the associated nanoscale phase separation microstructures on the mechanical properties, we carried out hardness measurements. Fig. 6 shows the Vickers microhardness (HV) and nanoindentation load-displacement curves for the cast samples. As can be seen, the sample cast at lower CRs has higher HV value (570 ± 18) compared to that in higher CR conditions (555 ± 18). Further, the load-displacement curves show that at a given load, the indentation depth for the sample cast under low CR conditions is smaller than the higher CR conditions, suggesting that higher strength achieved in the sample cast at lower CRs. The nanoindentation data reveal that hardness increases from 7.4 ± 0.19 GPa in 160 A (high CR) sample to 8.3 ± 0.2 GPa in 220 A (low CR). In addition, the elastic modulus value rises from 108.9 ± 1.9 GPa to 114 ± 2 GPa as higher melting currents were applied.

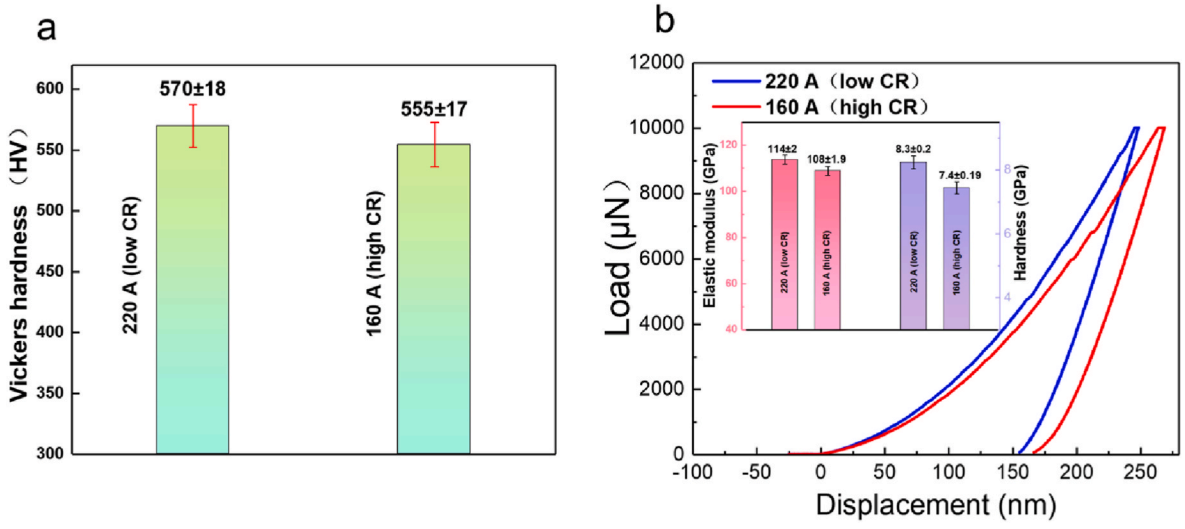

Fig. 6. (a) Vickers hardness comparison of 220 A (low CR) and 160 A (high CR) samples. (b) Typical nanoindentation load-displacement curves of the cast samples. The inset in (b) shows the hardness and elastic modulus of two samples.

A couple of reasons can explain the observation of increased strength (hardness) in the sample cast at lower CRs. First, the very fine nanocrystals precipitated during rapid quenching under low CR condition may be hard crystalline phases which increase the hardness compared to a fully amorphous structure (high CR conditions). Second, crystallization and phase separation both can decrease the free volume content of MG [33]. As the phase separation is more intense under low CR conditions [13] and nanoscale crystals exist in 220A (low CR) sample, a larger free volume content has been annihilated from the microstructure, yielding an increased hardness and decreased ΔH_{rel}. Third, the occurrence of phase separation enhances the atomic scale short-range ordering and correspondingly increases hardness [47], probably due to the formation of a higher fraction of Cu-Cu atomic pairs having smaller atomic radii compared to other atomic pairs in Cu–Zr–Al alloy system. And the short-range ordering is more favored in the sample cast at lower CRs, as confirmed by the lower FWHM values of the amorphous peak measured form the XRD patterns in Fig. 1. Finally, the size diversity among primary and secondary phase separated regions under low CR conditions may provide a stronger pinning effect on the formation of shear bands, thus inducing strain-hardening effect.

4. Conclusions

By using the XRD analysis, calorimetric measurements, electron microscopy characterizations, and mechanical testing the effects of quenching conditions on the phase separation of $Cu_{46}Zr_{46}Al_8$ BMG during copper-mold suction casting was investigated. The XRD analysis confirmed lower FWHM and higher degree of short-range ordering in the sample cast at higher melting currents (lower CRs). Calorimetric measurements showed that while thermal stability is not affected by the CR, higher values of $\Delta H_{cryst.}$ and ΔH_{rel} are attainable at higher CRs by decreasing the melting current. Additionally, the HRTEM images demonstrated that the microstructures of cast samples are strongly affected by the quenching condition. While the sample prepared at higher CRs contains primary droplet-type nanograins distributed uniformly throughout the fully amorphous matrix, the microstructure of the sample cast under low CR conditions revealed a two-stage phase separation microstructure, with coarsened primary-separated nanograins and small-sized secondary phase separated regions. The HAADF/STEM images and EDS analysis confirmed the primary and secondary separated regions are Cu-rich and the matrix is Cu-depleted. Moreover, higher hardness was observed for the sample cast at lower CRs, which was attributed to the higher degree of SRO, smaller free volume content, the existence of very fine nanocrystals, and different size scales of phase separated regions in this sample.

Author contributions

Conceptualization, S.S.; methodology, Z.Y. and S.S.; validation, Z.Y., R.S., S.S. and M.J.; formal analysis, R.S., Z.Y.; investigation, Z.Y., R.S., S. S.; resources, M.J.; data curation, Z.Y. and S.S.; writing—original draft preparation, Z.Y., S.S.; writing—review and editing, S.S., R.S., and M.J.; visualization, Z.Y., S.S.; supervision, M.J. and S.S.; project administration, M.J.; funding acquisition, M.J. All authors have read and agreed to the published version of the manuscript.

Funding

The work was supported by the Key Basic and Applied Research Program of Guangdong Province, China (Grant Nr. 2019B030302010), the NSF of China (Grant Nr. 52122105, 51871157, 51971150), the National Key Research and Development Program of China (Grant No. 2018YFA0703604). The authors also thank the assistance on microscope observation received from the Electron Microscope Center of the Shenzhen University.

Declaration of competing interest

The authors declare that they have no known competing financial interests or personal relationships that could have appeared to influence the work reported in this paper.

Data availability

Data will be made available on request.

References

[1] W.H. Wang, C. Dong, C.H. Shek, Bulk metallic glasses, Mater. Sci. Eng. R Rep. 44 (2–3) (2004) 45–89.
[2] E.S. Park, D.H. Kim, Phase separation and enhancement of plasticity in Cu–Zr–Al–Y bulk metallic glasses, Acta Mater. 54 (10) (2006) 2597–2604.
[3] Y. Dong, S. Liu, J. Biskupek, Q. Cao, X. Wang, J.-Z. Jiang, R. Wunderlich, H.-J. Fecht, Improved Tensile Ductility by Severe Plastic Deformation for Nano-Structured Metallic Glass, 2019. Materials.
[4] D.C. Hofmann, J.-Y. Suh, A. Wiest, G. Duan, M.-L. Lind, M.D. Demetriou, W. L. Johnson, Designing metallic glass matrix composites with high toughness and tensile ductility, Nature 451 (7182) (2008) 1085–1089.
[5] J. Qiao, H. Jia, P.K. Liaw, Metallic glass matrix composites, Mater. Sci. Eng. R Rep. 100 (2016) 1–69.
[6] I.V. Okulov, I.V. Soldatov, M.F. Sarmanova, I. Kaban, T. Gemming, K. Edström, J. Eckert, Flash Joule heating for ductilization of metallic glasses, Nat. Commun. 6 (1) (2015) 7932.
[7] S. Chen, H.-m. Fu, Z.-k. Li, L. Zhang, H.-w. Zhang, Z.-w. Zhu, H. Li, A.-m. Wang, Y.-d. Wang, H.-f. Zhang, Deformation behavior of Ta wire-reinforced Zr-based bulk metallic glass composites, J. Iron Steel Res. Int. 25 (6) (2018) 601–607.
[8] B. Sarac, Y.P. Ivanov, A. Chuvilin, T. Schöberl, M. Stoica, Z. Zhang, J. Eckert, Origin of large plasticity and multiscale effects in iron-based metallic glasses, Nat. Commun. 9 (1) (2018) 1333.
[9] S. Pauly, S. Gorantla, G. Wang, U. Kühn, J. Eckert, Transformation-mediated ductility in CuZr-based bulk metallic glasses, Nat. Mater. 9 (6) (2010) 473–477.
[10] X. Cui, X.F. Zhang, J.J. Li, F.Q. Zu, L.Z. Meng, J. Lu, F. Luo, Y.B. Ma, Centimeter-sized CuZrAl bulk metallic glass with good plasticity and chemical heterogeneity, Intermetallics 121 (2020), 106773.
[11] S. Sohrabi, M.C. Ri, H.Y. Jiang, L. Gu, P. Wen, Y.H. Sun, W.H. Wang, Prominent role of chemical heterogeneity on cryogenic rejuvenation and thermomechanical properties of La–Al–Ni metallic glass, Intermetallics 111 (2019), 106497.
[12] R. Rashidi, M. Malekan, R. Gholamipour, Microstructure and mechanical properties of a Cu-Zr based bulk metallic glass containing atomic scale chemical heterogeneities, Mater. Sci. Eng. 729 (2018) 433–438.
[13] D.H. Kim, W.T. Kim, E.S. Park, N. Mattern, J. Eckert, Phase separation in metallic glasses, Prog. Mater. Sci. 58 (8) (2013) 1103–1172.
[14] B.J. Park, H.J. Chang, D.H. Kim, W.T. Kim, In situ formation of two amorphous phases by liquid phase separation in Y–Ti–Al–Co alloy, Appl. Phys. Lett. 85 (26) (2004) 6353–6355.
[15] S. Liu, J. Ge, H. Ying, C. Lu, D. Ma, X.-L. Wang, X. Zuo, Y. Ren, T. Feng, J. Shen, H. Hahn, S. Lan, In situ scattering studies of crystallization kinetics in a phase-separated Zr–Cu–Fe–Al bulk metallic glass, Acta Metall. Sin. 35 (1) (2022) 103–114.
[16] K.B. Kim, J. Das, F. Baier, M.B. Tang, W.H. Wang, J. Eckert, Heterogeneity of a Cu47.5Zr47.5Al5 bulk metallic glass, Appl. Phys. Lett. 88 (5) (2006), 051911.
[17] J. Das, M. Tang, K. Kim, R. Theissmann, F. Baier, W. Wang, J. Eckert, Work-hardenable" ductile bulk metallic glass, Phys. Rev. Lett. 94 (20) (2005), 205501.
[18] L.Q. Xing, Y. Li, K.T. Ramesh, J. Li, T.C. Hufnagel, Enhanced plastic strain in Zr-based bulk amorphous alloys, Phys. Rev. B 64 (18) (2001), 180201.
[19] N. Nishiyama, A. Inoue, Glass-forming ability of bulk Pd40Ni10Cu30P20 alloy, Mater. Trans., JIM 37 (10) (1996) 1531–1539.
[20] A. Inoue, W. Zhang, T. Zhang, K. Kurosaka, High-strength Cu-based bulk glassy alloys in Cu–Zr–Ti and Cu–Hf–Ti ternary systems, Acta Mater. 49 (14) (2001) 2645–2652.
[21] A. Inoue, T. Zhang, T. Masumoto, Al, –La–Ni amorphous alloys with a wide supercooled liquid region, Mater. Trans., JIM 30 (12) (1989) 965–972.
[22] J.Y. Zhang, Z.Q. Zhou, Z.B. Zhang, M.H. Park, Q. Yu, Z. Li, J. Ma, A.D. Wang, H. G. Huang, M. Song, B.S. Guo, Q. Wang, Y. Yang, Recent development of chemically complex metallic glasses: from accelerated compositional design, additive manufacturing to novel applications, Mater, Futures 1 (1) (2022), 012001.
[23] H.-r. Jiang, X.-s. Wei, W.-f. Lu, D.-D. Liang, Z.-h. Wen, Z. Wang, H.-p. Xiang, J. Shen, Design of Cu-Zr-Al and Cu-Zr-Al-Sn bulk amorphous alloys with high glass-forming ability, J. Non-Cryst. Sol. 521 (2019), 119531.
[24] V.M. Villapún, F. Esat, S. Bull, L.G. Dover, S. González, Tuning the Mechanical and Antimicrobial Performance of a Cu-Based Metallic Glass Composite through Cooling Rate Control and Annealing, 2017. Materials.
[25] J. Pan, L. Liu, K.C. Chan, Enhanced plasticity by phase separation in CuZrAl bulk metallic glass with micro-addition of Fe, Scripta Mater. 60 (9) (2009) 822–825.
[26] N. Mattern, U. Vainio, J.M. Park, J.H. Han, A. Shariq, D.H. Kim, J. Eckert, Phase separation in Cu46Zr47−xAl7Gdx metallic glasses, J. Alloys Compd. 509 (2011) S23–S26.

[27] B. Sarac, J.T. Kim, Y.P. Ivanov, V. Soprunyuk, S.V. Ketov, W. Schranz, S.H. Hong, K.B. Kim, A.L. Greer, J. Eckert, Cryo-casting for controlled decomposition of Cu–Zr–Al bulk metallic glass into nanomaterials: implications for design optimization, ACS Appl. Nano Mater. (2021) 7771–7780.
[28] V.I. Tkatch, A.I. Limanovskii, S.N. Denisenko, S.G. Rassolov, The effect of the melt-spinning processing parameters on the rate of cooling, Mater. Sci. Eng., A 323 (1) (2002) 91–96.
[29] D.V. Louzguine-Luzgin, T. Saito, J. Saida, A. Inoue, Influence of cooling rate on the structure and properties of a Cu–Zr–Ti–Ag glassy alloy, J. Mater. Res. 23 (2) (2008) 515–522.
[30] S. Sohrabi, R. Gholamipour, Glass transition kinetics and fragility of ZrCuAlNi(Nb) metallic glasses, Intermetallics 145 (2022), 107532.
[31] D. Singh, R.K. Mandal, R.S. Tiwari, O.N. Srivastava, Effect of cooling rate on the crystallization and mechanical behaviour of Zr–Ga–Cu–Ni metallic glass composition, J. Alloys Compd. 648 (2015) 456–462.
[32] S. Lan, L. Zhu, Z. Wu, L. Gu, Q. Zhang, H. Kong, J. Liu, R. Song, S. Liu, G. Sha, Y. Wang, Q. Liu, W. Liu, P. Wang, C.-T. Liu, Y. Ren, X.-L. Wang, A medium-range structure motif linking amorphous and crystalline states, Nat. Mater. 20 (10) (2021) 1347–1352.
[33] Q.P. Cao, J.F. Li, Y.H. Zhou, A. Horsewell, J.Z. Jiang, Free-volume evolution and its temperature dependence during rolling of Cu60Zr20Ti20 bulk metallic glass, Appl. Phys. Lett. 87 (10) (2005), 101901.
[34] Y. Sun, A. Concustell, A.L. Greer, Thermomechanical processing of metallic glasses: extending the range of the glassy state, Nat. Rev. Mater. 1 (2016), 16039.
[35] S. Sohrabi, B.Y. Sun, M. Mahmoodan, Y.H. Sun, R. Gholamipour, W.H. Wang, Rejuvenation by compressive elasto-static loading: the role of static stress on a Zr-based metallic glass, J. Alloys Compd. 933 (2023), 167715.
[36] A.L. Greer, Y.H. Sun, Stored energy in metallic glasses due to strains within the elastic limit, Philos. Mag. A 96 (16) (2016) 1643–1663.
[37] A. Slipenyuk, J. Eckert, Correlation between enthalpy change and free volume reduction during structural relaxation of Zr55Cu30Al10Ni5 metallic glass, Scripta Mater. 50 (1) (2004) 39–44.
[38] L. Battezzati, G. Riontino, M. Baricco, A. Lucci, F. Marino, A DSC study of structural relaxation in metallic glasses prepared with different quenching rates Proceedings of the Fifth International Conference on Liquid and Amorphous Metals, J. Non-Cryst. Sol. 61 (1984) 877–882.
[39] B.B. Sun, Y.B. Wang, J. Wen, H. Yang, M.L. Sui, J.Q. Wang, E. Ma, Artifacts induced in metallic glasses during TEM sample preparation, Scripta Mater. 53 (7) (2005) 805–809.
[40] G. Kumar, T. Ohkubo, T. Mukai, K. Hono, Plasticity and microstructure of Zr–Cu–Al bulk metallic glasses, Scripta Mater. 57 (2) (2007) 173–176.
[41] S. Venkataraman, K. Biswas, B.C. Wei, D.J. Sordelet, J. Eckert, On the fragility of Cu 47 Ti 33 Zr 11 Ni 8 Si 1 metallic glass, J. Phys. D Appl. Phys. 39 (12) (2006) 2600.
[42] S. Lan, Z. Wu, X. Wei, J. Zhou, Z. Lu, J. Neuefeind, X.-L. Wang, Structure origin of a transition of classic-to-avalanche nucleation in Zr-Cu-Al bulk metallic glasses, Acta Mater. 149 (2018) 108–118.
[43] Q.P. Cao, J.F. Li, Y.H. Zhou, A. Horsewell, J.Z. Jiang, Effect of rolling deformation on the microstructure of bulk Cu60Zr20Ti20 metallic glass and its crystallization, Acta Mater. 54 (16) (2006) 4373–4383.
[44] F. Sommer, Association model for the description of thermodynamic functions of liquid alloys: II. Numerical treatment and results, Int. J. Mater. Res. 73 (2) (1982) 77–86.
[45] A.A. Kündig, M. Ohnuma, D.H. Ping, T. Ohkubo, K. Hono, In situ formed two-phase metallic glass with surface fractal microstructure, Acta Mater. 52 (8) (2004) 2441–2448.
[46] K.I. Dragnevski, A.M. Mullis, R.F. Cochrane, The effect of experimental variables on the levels of melt undercooling, Mater. Sci. Eng., A 375–377 (2004) 485–487.
[47] Q. Cao, J. Li, Y. Zhou, J. Jiang, Mechanically driven phase separation and corresponding microhardness change in Cu60Zr20Ti20 bulk metallic glass, Appl. Phys. Lett. 86 (8) (2005), 081913.